micromachines

Article

An Investigation into the Densification-Affected Deformation and Fracture in Fused Silica under Contact Sliding

Changsheng Li [1,2], Yushan Ma [3], Lin Sun [1,*], Liangchi Zhang [4,5,6], Chuhan Wu [7], Jianjun Ding [1,*], Duanzhi Duan [1], Xuepeng Wang [3] and Zhandong Chang [3]

1 State Key Laboratory for Manufacturing Systems Engineering, Xi'an Jiaotong University, Xi'an 710049, China; li.changsheng@xjtu.edu.cn (C.L.); dzduan@163.com (D.D.)
2 State Key Laboratory of Mechanical System and Vibration, Shanghai Jiaotong University, Shanghai 200240, China
3 Wuzhong Instrument Co., Ltd., Wuzhong 751199, China; mys@wzyb.com.cn (Y.M.); 18729961058@163.com (X.W.); czd@wzyb.com.cn (Z.C.)
4 Shenzhen Key Laboratory of Cross-scale Manufacturing Mechanics, Southern University of Science and Technology, Shenzhen 518055, China; zhanglc@sustech.edu.cn
5 SUSTech Institute for Manufacturing Innovation, Southern University of Science and Technology, Shenzhen 518055, China
6 Department of Mechanics and Aerospace Engineering, Southern University of Science and Technology, Shenzhen 518055, China
7 School of Mechanical and Manufacturing Engineering, The University of New South Wales, Sydney, NSW 2052, Australia; chuhan.wu@unsw.edu.au
* Correspondence: sunlin@xjtu.edu.cn (L.S.); dianjianjun@126.com (J.D.)

check for updates

Citation: Li, C.; Ma, Y.; Sun, L.; Zhang, L.; Wu, C.; Ding, J.; Duan, D.; Wang, X.; Chang, Z. An Investigation into the Densification-Affected Deformation and Fracture in Fused Silica under Contact Sliding. *Micromachines* **2022**, *13*, 1106. https://doi.org/10.3390/mi13071106

Academic Editors: Chengwei Kang, Chunjin Wang and Jiang Guo

Received: 30 June 2022
Accepted: 9 July 2022
Published: 14 July 2022

Publisher's Note: MDPI stays neutral with regard to jurisdictional claims in published maps and institutional affiliations.

Abstract: Subsurface damage of fused silica optics is one of the major factors restricting the performance of optical systems. The densification-affected deformation and fracture in fused silica under a sliding contact are investigated in this study, via three-dimensional finite element analysis (FEA). The finite element models of scratching with 70.3° conical and Berkovich indenters are established. A refined elliptical constitutive model is used to consider the influence of densification. The finite element models are experimentally verified by elastic recovery, and theoretically verified by hardness ratio. Results of densification and plastic deformation distributions indicate that the accuracy of existent sliding stress field models may be improved if the spherical/cylindrical yield region is replaced by an ellipsoid/cylindroid, and the embedding of the yield region is considered. The initiation sequence, and the locations and stages of radial, median, and lateral cracks are discussed by analyzing the predicted sliding stress fields. Median and radial cracks along the sliding direction tend to be the first cracks that emerge in the sliding and unloading stages, respectively. They coalesce to form a big median–radial crack that penetrates through the entire yield region. The fracture behavior of fused silica revealed in this study is essential in the low-damage machining of fused silica optics.

Keywords: sliding contact; fused silica; densification; finite element analysis; cracks

1. Introduction

Fused silica, or silica-rich glass optics, are widely used in laser nuclear fusion devices [1], large astronomical telescopes [2], semiconductor technology [3,4], and consumer electronics. Subsurface damage has plenty of negative effects on the performance of optics, e.g., increasing optical scatter, reducing mechanical strength, and increasing laser-induced damage (LID). For instance, the subsurface damage is one of the precursors resulting in LID. The LID of fused silica optics is one of the key factors restricting the output power and a key challenge for the long-term and stable operation of high-power laser facilities [5]. Therefore, an in-depth understanding of the material removal and damage formation mechanisms of fused silica subjected to machining is essential to fabricate damage-free optics.

Fused silica optics are generally fabricated by abrasive grain-based methods, e.g., grinding and polishing. Therefore, indentation/scratching mechanics are widely used to study the fracture of fused silica subjected to machining [6,7]. In addition to the contact pressure between the indenter and the sample, the indentation stress field also results from a misfit between the plastic zone beneath the indentation and the surrounding elastic matrix. Therefore, the elastic indentation models, e.g., the classical Boussinesq solution and Hertzian field [8] for elastic contact, are insufficient. Later on, Hill et al. [9] developed a model for the wedge indentation of the rigid–perfectly-plastic materials. However, this model is not suitable for indentation with blunt indenters, or with materials with a low ratio of Young's modulus to yield stress. To this end, Johnson et al. [10] proposed the expanding-cavity model that treats the indentation-induced plastic zone as an expanding zone. This model was successfully used by Lawn et al. [11] to analyze the indentation damage in ceramics.

Different from most materials, fused silica suffered from significant permanent volume contraction under high hydrostatic pressure. This phenomenon is known as densification [12]. The aforementioned indentation stress field models ignore the influence of densification, which limits the accuracy for fused silica. In order to solve this problem, Yoffe [13] proposed the Blister stress field model, which, for the first time, integrates the material densification. Li et al. [14] modified the ECD model to make it suitable for materials with densification. Compared with the Yoffe model, the modified ECD model considers the distribution characteristics of the contact pressure between the indenter and the sample. In addition, the center of the plastic zone is not restricted in the sample surface.

The grinding and polishing processes are more analogous to successive scratching compared with indentations. The studies on analytical sliding stress fields are rather limited. Hamilton and Goodman [15] proposed an elastic model for sliding contact. Ahn et al. [16] developed the sliding blister stress field model by extending the Yoffe model to scratching, in which the plastic deformation and material densification were considered. Similar models were used to analyze the cracking behavior of BK7 glass [17], fused silica [17], and silicon [18] subjected to scratching. However, these models assume that the indenter is conical and the center of plastic zone locates in the sample surface, which limits the prediction accuracy.

The finite element method is a powerful tool to investigate the deformation, friction [19], wear [20], and fracture [21] of brittle materials subjected to scratching. It should be noted, however, that in these studies the constitutive models used were either purely elastic or von Mises [22], and that the effects of material densification were neglected. Imaoka et al. [23] and Gadelrab et al. [24] developed the positive linear models to consider densification. The mean hydrostatic stress is linear with the equivalent shear stress in these models. Xin et al. [25] proposed a negative linear model to explain the unique features of fused silica during grinding and polishing. Kermouche et al. [26] proposed an elliptical constitutive model to consider the shear-assisted densification. This model considers the hardening of yield pressure with densification, which is neglected in the linear models. The elliptical model is widely used to investigate the indentation deformation and fracture in fused silica [12,27]. Later on, the elliptical constitutive model was refined by Li et al. [28], to consider the influence of densification on elastic properties and the saturation of densification with hydrostatic pressure. This refined elliptical model was successfully used to study the indentation mechanisms [28,29] and sliding friction behavior [30].

This paper aims to establish three-dimensional finite element models for conical and Berkovich scratching using the refined elliptical model. Finite element simulations are performed to investigate the densification and deformation in fused silica subjected to scratching to reveal the stress field more precisely. The influence of friction on indentation and scratching hardness is investigated, and the cracking behavior of fused silica under scratching explored.

2. Scratching Tests

As shown in Figure 1, fused silica samples (Corning UV 7980, Corning Corp., Corning, NY, USA) were scratched by an edge-forward Berkovich tip on a nanoindentation machine (TI-950 TriboIndenter, Hysitron Inc., Eden Prairie, MN, USA). The samples were carefully polished to achieve a surface roughness small than 2 nm. Scratching tests were performed under constant normal loads of 1 mN, 2 mN, 4 mN, 200 mN, 400 mN, 600 mN, 1 N, and 1.2 N. The sliding length was 250 μm, which is significantly greater than the scratching depth. The scratching process consists of the approaching stage Ⓐ, the preliminary profiling stage Ⓑ (to obtain the original surface profile), the indentation stage Ⓒ, the scratching stage Ⓓ, the unloading stage Ⓔ, and the postmortem profiling stage Ⓕ (to obtain the residual surface profile). The variations of normal load, normal displacement, lateral load, and lateral displacement with time were recorded during scratching.

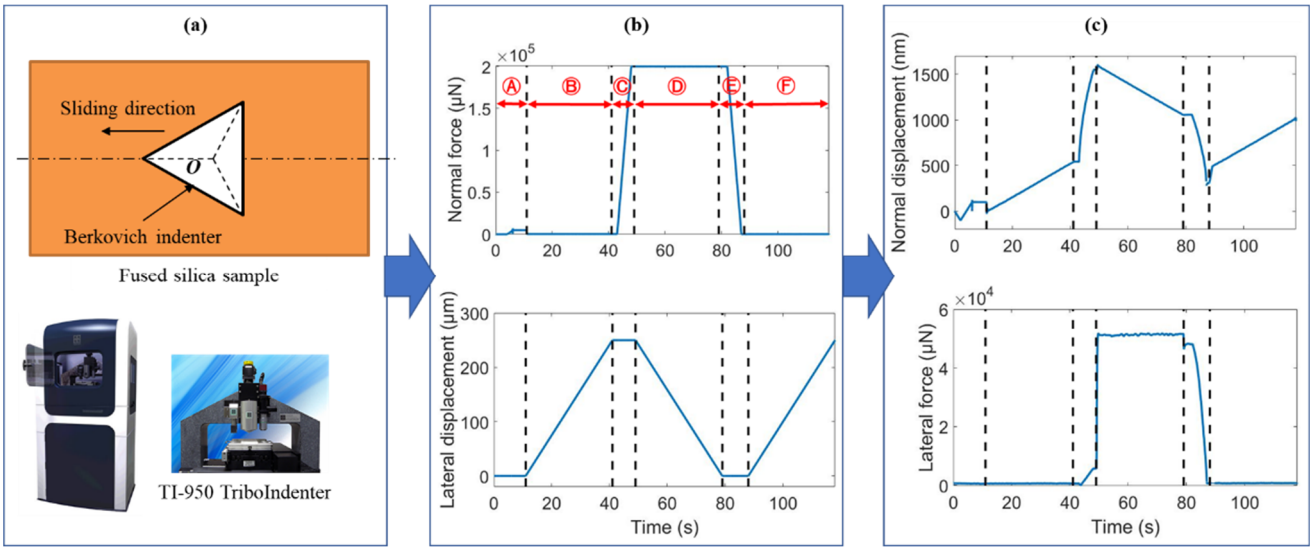

Figure 1. (**a**) Schematic diagram of edge-forward Berkovich scratching, (**b**) the applied normal force and lateral displacement for the normal load of 200 mN, and (**c**) the resulting normal displacement and lateral force.

After scratching, the samples were measured by an atomic force microscope (AFM) (Innova, Veeco, Plainview, NY, USA) to obtain the three-dimensional topography of the impression. After etching by the buffered HF solution to open the surface cracks [31], the morphology of the cracks was characterized by a scanning electron microscope (SEM) (SU3500, Hitachi, Japan).

3. Finite Element Modeling

The finite element analysis of scratching with an edge-forward Berkovich indenter and a conical indenter was performed on a commercial finite element code ABAQUS. A modified elliptical constitutive model [28,30] was used to consider the influence of densification on the deformation in fused silica:

$$f(\sigma_{ij}) = \left(\frac{q}{d}\right)^2 + \left(\frac{p}{p_b}\right)^2 - 1 = 0 \quad (1)$$

where q is equivalent shear stress; p is hydrostatic pressure; d is the von Mises yield stress under pure shear; and p_b is the hydrostatic yield stress for pure compression. The relationship between hydrostatic pressure p and the densification ζ is modeled by:

$$\zeta = \frac{\zeta_{\max}}{1 + e^{-k(p-p_0)}} \quad (2)$$

where ζ_{max} (%) is the saturated densification under compression, and p_0 (GPa) is the hydrostatic pressure under which a densification of $\zeta_{max}/2$ is produced. The parameters of the modified elliptical model used in this study are taken from the ref. [28].

In the finite element model, an infinitely sharp Berkovich edge-forward indenter slides along the x-axis on the top surface of a deformable parallelepiped with a dimension of $W \times W \times (l + 2W)$, as shown in Figure 2. The diamond indenter is assumed to be rigid because its Young's modulus [32] and hardness [33] are much higher than those of the fused silica samples [14]. An eight-node linear brick element with reduced integration and hourglass control is used. Refined FE mesh with an element size of l_e is used in a parallelepiped with a dimension of $a \times a \times (l + 2W)$, and graded FE mesh is used in the residual region. For conical scratching, the semi-included angle α of the conical indenter is set as 70.3°, to ensure that the projected area-to-indentation depth function is the same as the commonly used Vickers and Berkovich indenters. $A = 2.79\ h_{max}$ is the nominal contact radius for 70.3° conical scratching.

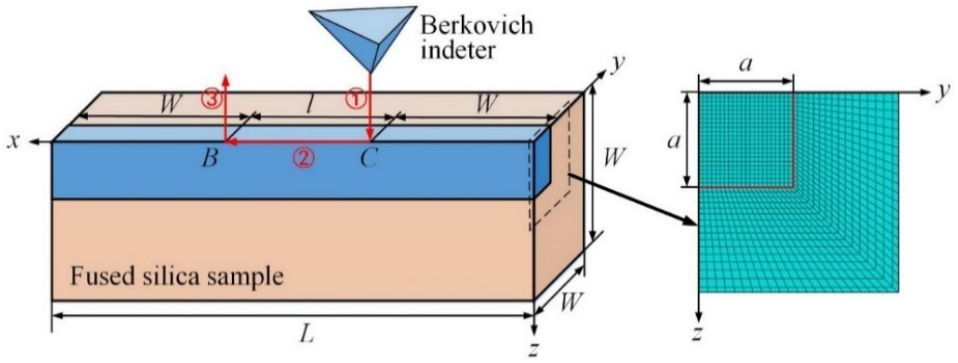

Figure 2. The finite element model of scratching with a Berkovich indenter.

As shown in Figures 2 and 3, the sliding process is divided into three stages, i.e., the indentation stage ①, the sliding stage ②, and the unloading stage ③. The scratching depth, length, and speed are denoted as h_{max}, l, and v, respectively. The Coulomb friction model is used to model the adhesion friction behavior between the indenter and the sample. The coefficient of adhesion friction f was determined to be 0.04, by comparing FEA and scratching tests.

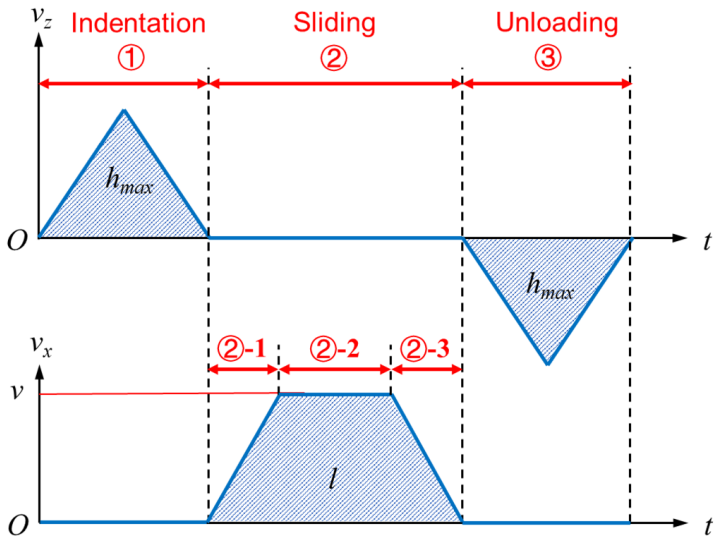

Figure 3. The velocity of the indenter during the FEA of scratching.

The single-variable method is used to optimize the cross-section dimension W, sliding length l, and element size l_e. The appropriate parameters result in stable and convergent normal and tangential loads, and apparent coefficient of friction in the sliding stage. h_{max} is assumed to be 1 μm. Results show that a cross-section dimension of $5a \times 5a$, a sliding length of 10 h_{max}, and a mesh size of 1/8 h_{max} are appropriate for the simulations.

4. Verification of Finite Element Models

4.1. Experimental Verification of Elastic Recovery

The elastic recovery ratio f_e for scratching reflects the extent of elastic deformation relative to the whole deformation. In addition, f_e can be conveniently measured by AFM. Therefore, f_e is used to verify the finite element model in this study.

As shown in Figure 4, the leading end of the impression induced by scratching with an edge-forward Berkovich indenter is measured by AFM to obtain its three-dimensional topography. Pile-up is obvious on the lateral sides of the impression. Figure 4 also indicates that the residual depth h_f (see Figure 5) slightly decreases with the distance d to the unloading position of indenter tip. The profile shown in Figure 5 is obtained by averaging five equally spaced cross-section profiles of the middle part of the impression. The residual scratch depth h_f after elastic recovery, determined from Figure 5, is 668 nm.

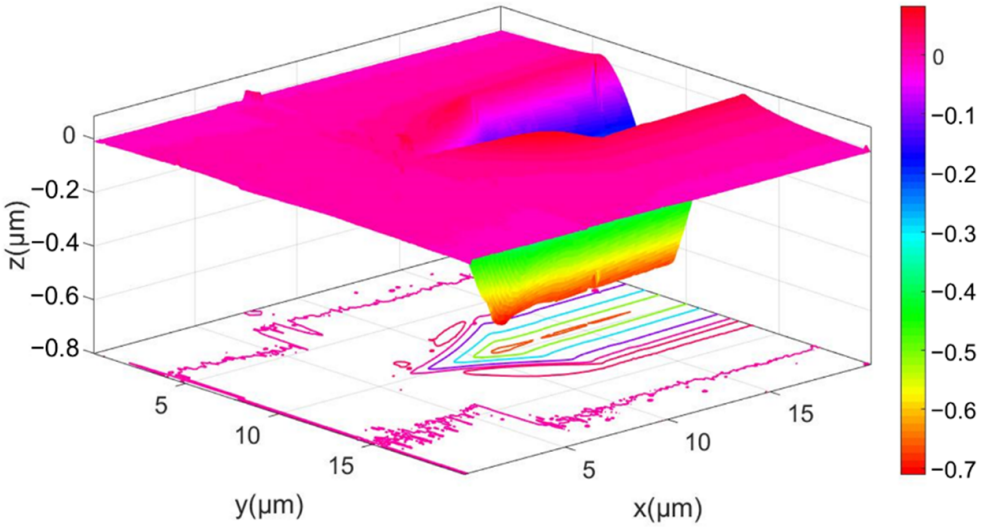

Figure 4. The AFM-measured three-dimensional topography of the scratching impression induced by an edge-forward Berkovich indenter under the normal load of 200 mN.

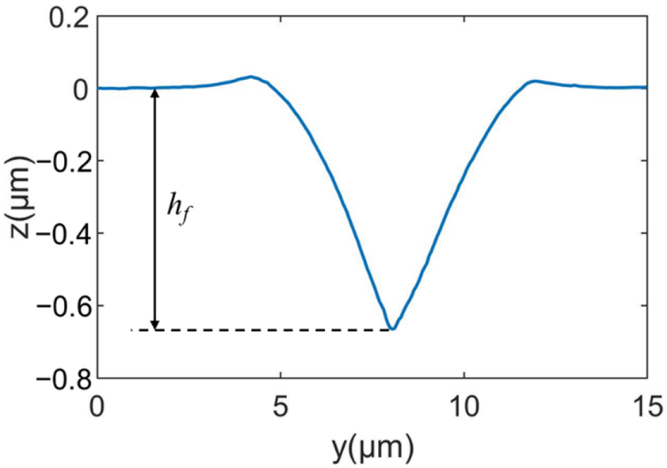

Figure 5. The average cross-section profile of the scratching impression.

In order to determine the scratching depth directly from the displacement curve, the normal displacement of the indenter (see Figure 1c) during the scratching process was corrected by the original profile of the sample surface. The corrected normal displacement in the scratching stage Ⓓ was calculated by subtracting the uncorrected displacement from t_2 to t_1 in the stage Ⓑ from the uncorrected displacement from t_3 to t_4. Similarly, the corrected normal displacement in the postmortem profiling stage Ⓕ was calculated by subtracting the uncorrected displacement from t_1 to t_2 from the uncorrected displacement from t_5 to t_6. The evolution of the corrected normal displacement with time is shown in Figure 6. The maximum scratching depth and residual depth are 1063 nm and 479 nm, respectively. It is worth noting that this value of residual depth is smaller than that measure by AFM (i.e., h_f = 668 nm). This is possibly because the indenter did not strictly follow the scratching path in stage Ⓕ, due to the movement of the sample or the motion error of the indentation test in the lateral direction. By contrast, the AFM probe accurately detects the lowest positions of the residual scratching profiles for two reasons. First, the tip radius of the AFM probe is much smaller than that of the Berkovich indenter. Second, the AFM probe is scanning across the impression. Using the AFM-measured h_f, the elastic recovery ratio is calculated to be $f_e = 1 - h_f/h_{amx}$ = 37.2%. Ba analyzing the FEA-predicted profiles of the scratching impression at the fully-loaded and fully-unloaded states shown in Figure 7, the value of f_e predicted by FEA is 37%, which is very close to the experimental value.

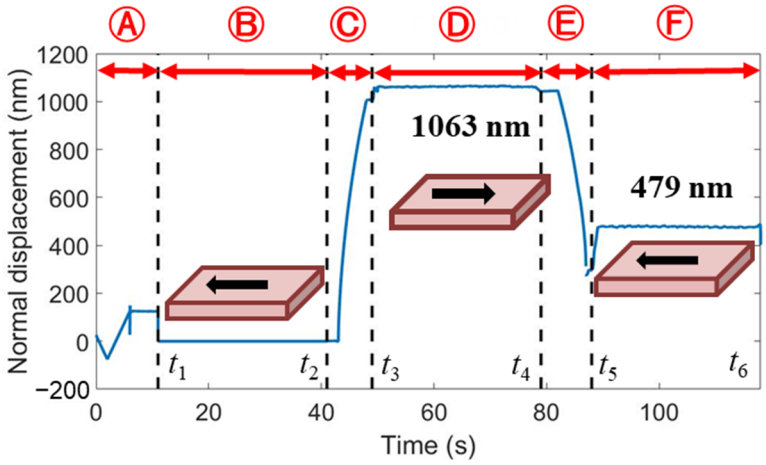

Figure 6. The evolution of the corrected normal displacement with time for scratching with an edge-forward Berkovich indenter, under the normal load of 200 mN.

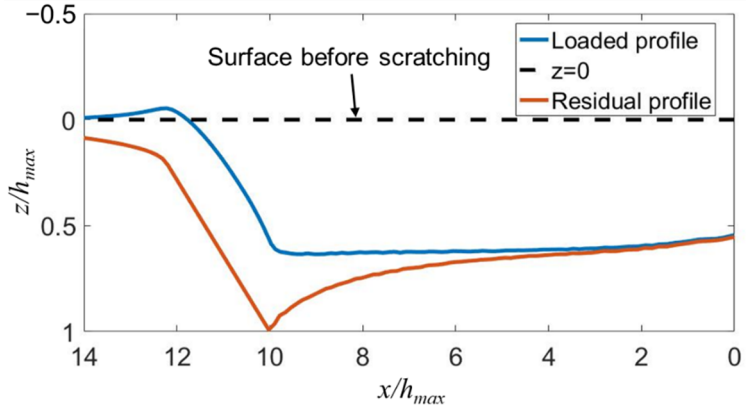

Figure 7. The FEA-simulated profiles of the scratching impression at the fully loaded and fully unloaded states for an edge-forward Berkovich indenter.

4.2. Theoretical Verification of Hardness Ratio

As shown in Figure 8, FEA predicts that the hardness ratio $k_H^p = H_T^p / H_s^p$ is slightly larger than utility, and nearly independent of the sharpness of the indenter, where H_T^p and H_s^p are the ploughing hardness along the sliding and vertical directions, respectively. This is consistent with theoretical analysis, as detailed below.

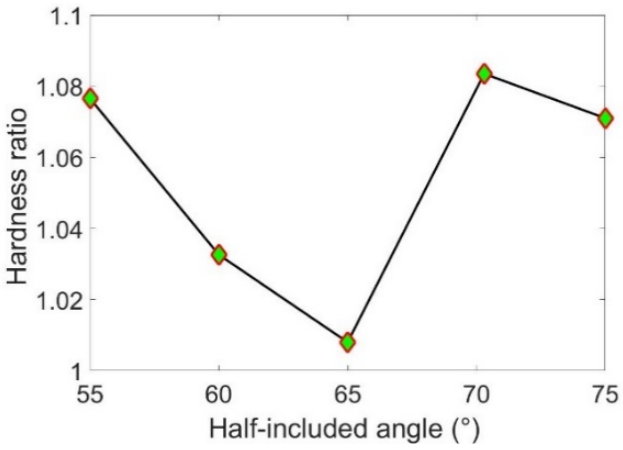

Figure 8. The variation of hardness ratio k_H^p with the half-included angle of the conical indenters.

For an infinitesimal contact area dA, the contact force is normal to dA. Therefore, the forces along the sliding and vertical directions, i.e., dF_T and dF_N, have the following relationship:

$$\frac{dF_T}{dA_{pl}} = \frac{dF_N}{dA_{pv}} = p(h, \beta) \tag{3}$$

where A_{pl} and A_{pv} are the laterally and vertically projected contact areas, respectively; $p(h,\beta)$ is the contact pressure at the point (h,β) on the indenter surface; and β and h are the phase and the height measured from the indenter tip, respectively. According to the definition of hardness, the ploughing hardness can be expressed by:

$$H_s^p = \frac{\int p(h,\beta) dA_{pv}}{A_{pv}} \tag{4}$$

and

$$H_T^p = \frac{\int p(h,\beta) dA_{pl}}{A_{pl}} \tag{5}$$

The contours of the contact stress induced by conical scratching and Berkovich scratching resemble concentric circles and triangles, respectively [30]. Therefore, $p(h,\beta)$ is nearly independent of β. As the geometries of the conical and Berkovich indenters are self-similar, the vertically and laterally projected areas of the contact zone with a height from h to $h + dh$, i.e., $dA_{pl,h\sim h+\Delta h}$ and $dA_{pv,h\sim h+\Delta h}$ have the following relationship:

$$\frac{dA_{pl,h\sim h+\Delta h}}{dA_{pv,h\sim h+\Delta h}} \approx \frac{A_{pl}}{A_{pv}} \tag{6}$$

Therefore, the hardness ratio:

$$k_H^p = \frac{H_T^p}{H_s^p} = \frac{\int_{h=0}^{h_c} p(h) dA_{pl,h\sim h+\Delta h}}{\int_{h=0}^{h_c} p(h) dA_{pv,h\sim h+\Delta h}} \cdot \frac{A_{pv}}{A_{pl}} \approx 1 \tag{7}$$

By combining Equations (3), (12) and (18) in ref. [30], the following expression can be obtained for a conical indenter:

$$\frac{k_H}{k_H^p} \approx 1 + \frac{f}{\mu_0 \sin \alpha} \tag{8}$$

where $k_H = H_T/H_s$ is the ratio of tangential hardness and scratching hardness; and μ_0 is the friction coefficient induced by ploughing. As $k_H^p \approx 1$, we can conclude from Equation (8) that $k_H > 1$ when friction exists, i.e., $H_T > H_s$. This is consistent with the scratching tests [34]. It is worth noting that the above analysis considers the non-uniform distribution of the contact pressure. This is more accurate than the widely adopted assumption that the contact pressure is uniformly distributed [35].

5. Deformation and Fracture in Fused Silica under Scratching

5.1. Scratching Hardness

Scratching hardness is widely used to model the scratching load that is a key factor determining the fracture behavior. Although it is reported that friction only plays a small role in indentation hardness for blunt indenters [36], Figure 9 shows that the indentation hardness H_i (the hardness at the end of stage ①) for edge-leading Berkovich scratching is slightly increased with the rise in friction. By contrast, the scratching hardness (the hardness in the right red box) is nearly independent of friction.

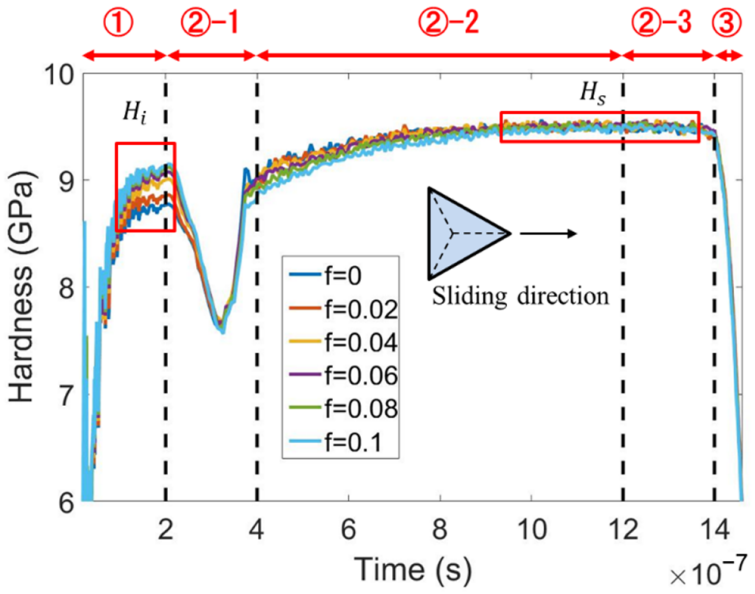

Figure 9. The variation of hardness with time at various values of adhesion friction coefficient f for edge-leading Berkovich scratching.

In order to understand the above phenomena, the evolutions of the contact area and normal force with time are plotted in Figure 10a,b, respectively. During the transition from indentation to sliding, i.e., in the stage ②-1, the contact area is considerably reduced because the support for the indenter rear is removed. If no elastic recovery occurs, the rear face of the indenter is entirely separated from the sample surface, and the contact area decreases to two-thirds. However, Figure 10a shows that the contact area during the steady sliding stage (in the right red box) is significantly bigger than two-thirds of that during indentation (in the left red box). This is due to elastic recovery.

The moving direction of the indenter relative to the sample determines the influence of friction on the contact area. The contact area during static indentation is slightly decreased by friction, because the friction-induced downward shear stress applied to the sample surface results in a decrease in the contact area, as shown in Figure 10a. By contrast, friction

leads to an increase in the contact area during the steady sliding stage because the friction-induced shear stress on the sample surface is upward. The indentation hardness increases with friction, while the contact area decreases with friction. Therefore, the normal force during indentation is nearly independent of friction, as shown in Figure 10b. During the steady sliding stage, the scratching hardness is nearly independent of friction because the friction increases both the contact area and the normal force.

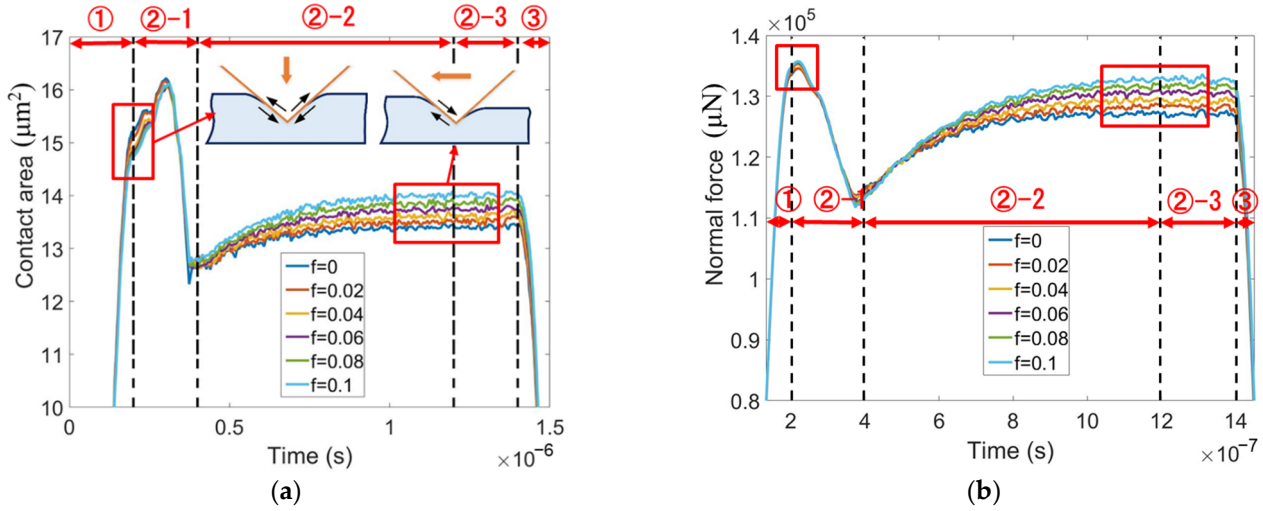

Figure 10. The evolutions of (**a**) contact area and (**b**) normal force with time at various friction coefficients for edge-leading Berkovich scratching.

Although the scratching hardness H_s for Berkovich indenter is independent of f, H_s for conical indenter is linearly decreased with f, as demonstrated in Figure 11. The scratching hardness induced by ploughing, i.e., H_s^p, remains nearly unchanged when f increases from 0 to 0.2.

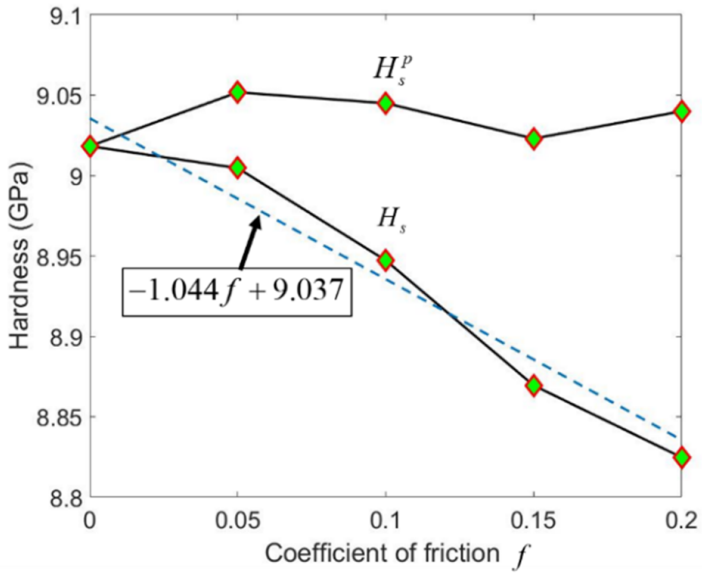

Figure 11. The hardness during scratching as a function of adhesion friction coefficient f for scratching with a 70.3° conical indenter. The value pairs of (H_s, f) is fitted to obtain the dash line.

5.2. Plastic Deformation

It is reported that the stress and deformation are relieved by densification [13,25]. The stress distribution is significantly influenced by the geometry and location of the elastic–plastic boundary [14,37]. In the analytical models of sliding stress fields, e.g., the Ahn

model [16] and the Wang model [17], the plastic region is assumed to be a sphere with the center on the sample surface.

As shown in Figure 12, the maximum densification locates in the region that the indenter tip passes. The maximum value of densification predicted by FEA, i.e., 22.6%, is close to the measured saturated densification, i.e., 21% [38]. By comparing the densification contours in the top surface and the *xz*-cross-section shown in Figure 12, it is found that the contours in the *yz*-cross-sections are flat ellipses. Figure 12 also indicates that the densification in fused silica caused by scratching is bigger than that caused by indentation.

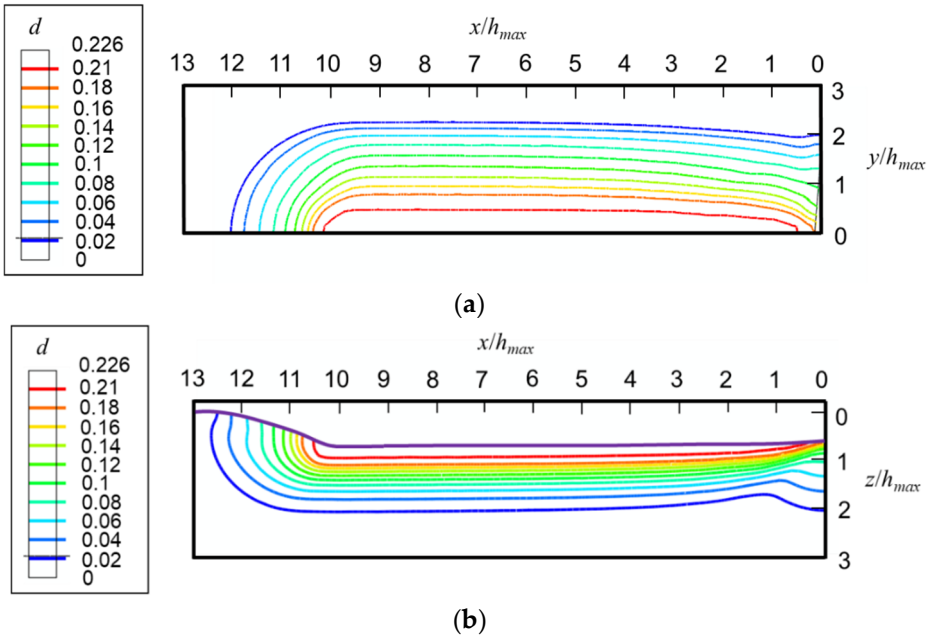

Figure 12. Contours of densification at the fully unloaded state induced by scratching with a 70.3° conical indenter in (**a**) the top surface and (**b**) *xz*-cross-section.

Figure 13a shows that the elastic–plastic boundary in fused silica induced by scratching deviates from a circle. By contrast, Figure 13b demonstrates that the boundary can be tightly fitted by an ellipse. Figures 13 and 14 indicate that the yield region is an ellipsoid in the front of the indenter ($x/h_{max} > 10$), and a cylindroid at the rear of the indenter ($x/h_{max} \leq 10$).

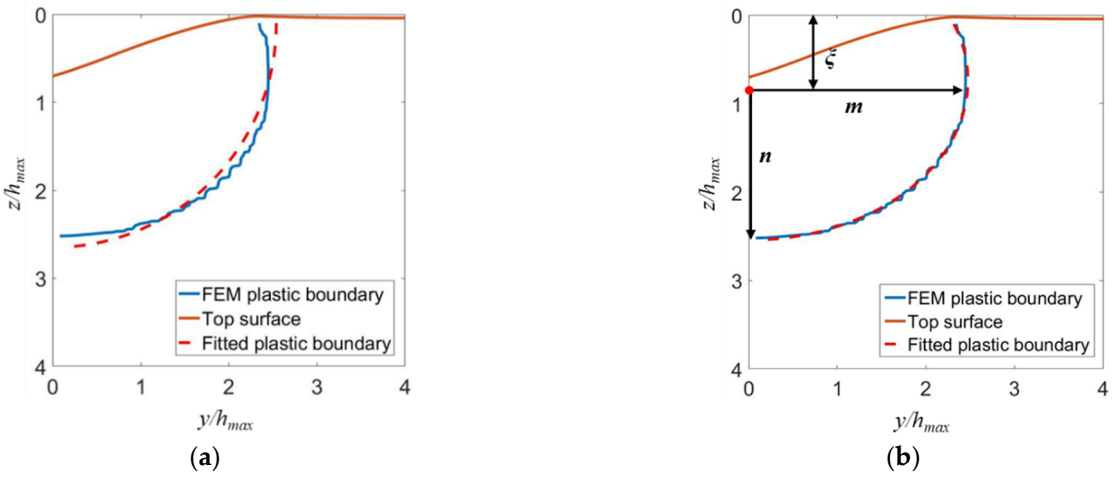

Figure 13. The elastic–plastic boundaries defined by a von Mises equivalent plastic strain of 10^{-2} in the *yz*-cross-section at the fully unloaded state for 70.3° conical scratching. The simulated boundaries are fitted by (**a**) a circular arc and (**b**) an elliptical arc.

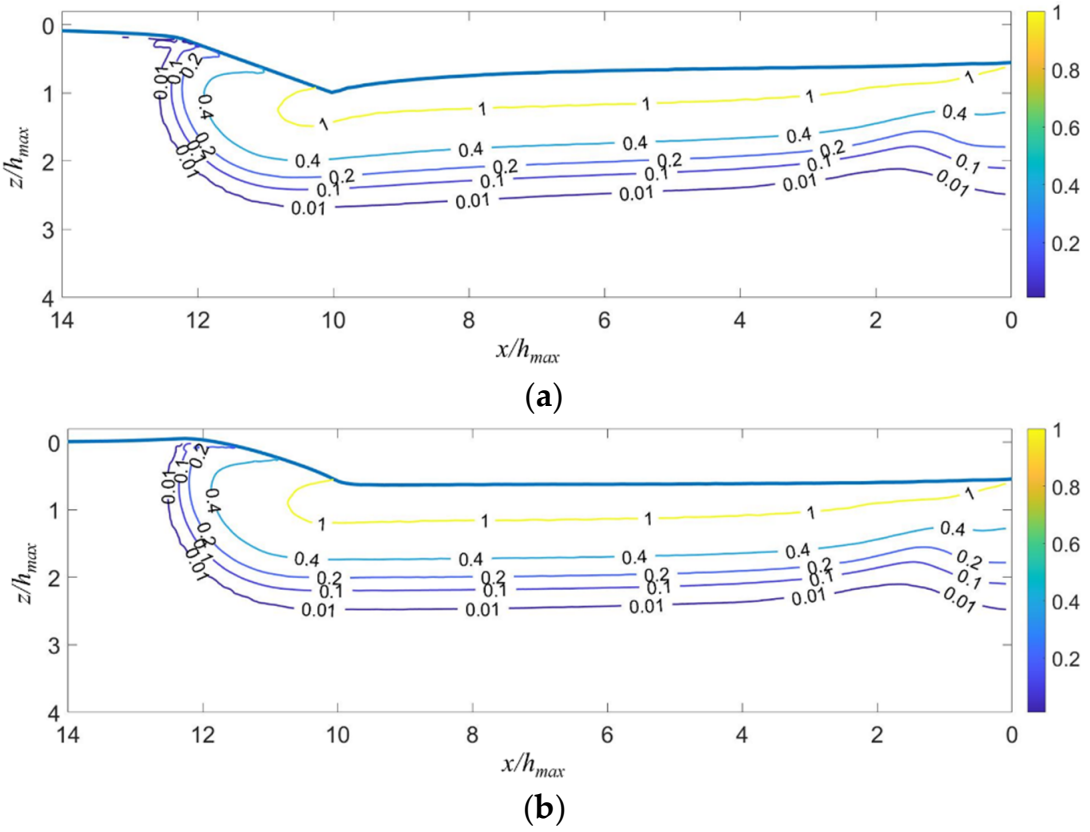

Figure 14. The contours of von Mises equivalent plastic strain in the *xz*-cross-section (**a**) at the fully loaded and (**b**) fully unloaded states.

As shown in Figure 13b, the shape of the elastic–plastic boundary is characterized by the length m of the semi-major axis, the length n of the semi-minor axis, and the depth ξ of the elastic–plastic boundary center. The semi-major and semi-minor axes are along the lateral and vertical directions, respectively. These parameters can be determined by fitting the elastic–plastic boundary by the following formula:

$$\left(\frac{y}{m}\right)^2 + \left(\frac{z-\xi}{n}\right)^2 = 1 \tag{9}$$

The fitted results are shown in Figure 15. The real contact radius a_r predicted by FEA equals 2.24 h_{max}. Figure 15a shows that m is bigger than a, while n is smaller than a. After unloading, m remains nearly unchanged, but n in the cross-section close to point B increases, due to the significant elastic recovery. m is significantly larger than n in the steady sliding stage. Therefore, the prediction accuracy of the existent sliding stress field models may be greatly improved if the spherical/cylindrical yield region is replaced by an ellipsoid/cylindroid. Figure 15b shows that the depth of the elastic–plastic boundary center in the *yz*-cross-section behind the indenter decreases rapidly when the indenter moves far away from it. ξ for scratching is much bigger than that for indentation (close to ξ at l_B = 9.5 h_{max}) at both the fully loaded and the fully unloaded states. This indicates that the Ahn and Wang models should be refined to allow for the embedding of the center of the plastic zone.

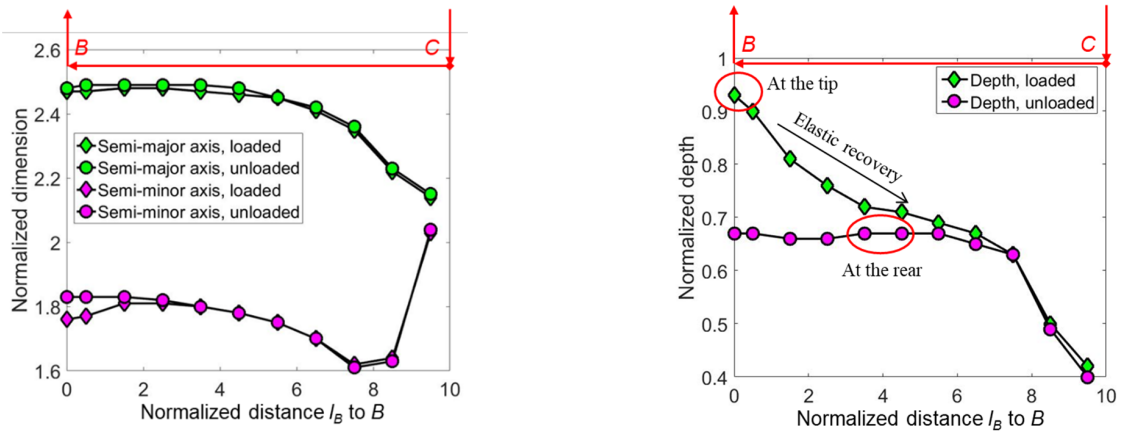

Figure 15. The fitted (**a**) dimension and (**b**) depth of the elastic–plastic boundary normalized by h_{max}. The indenter moves from the point *C* to the point *B* in the scratching stage (see Figure 2).

5.3. Stress Fields and Cracking Behavior

5.3.1. In the Sliding Stage

The scratching-induced stress contours under a conical indenter at the end of the sliding stage ② are shown in Figure 16. In the front of the indenter tip, i.e., in the region $x \geq 0$, the shape of the contour lines induced by scratching is similar to those induced by indentation [29]. By contrast, at the back of the indenter tip, the contours are flattened, due to the plastic deformation left by the sliding indenter.

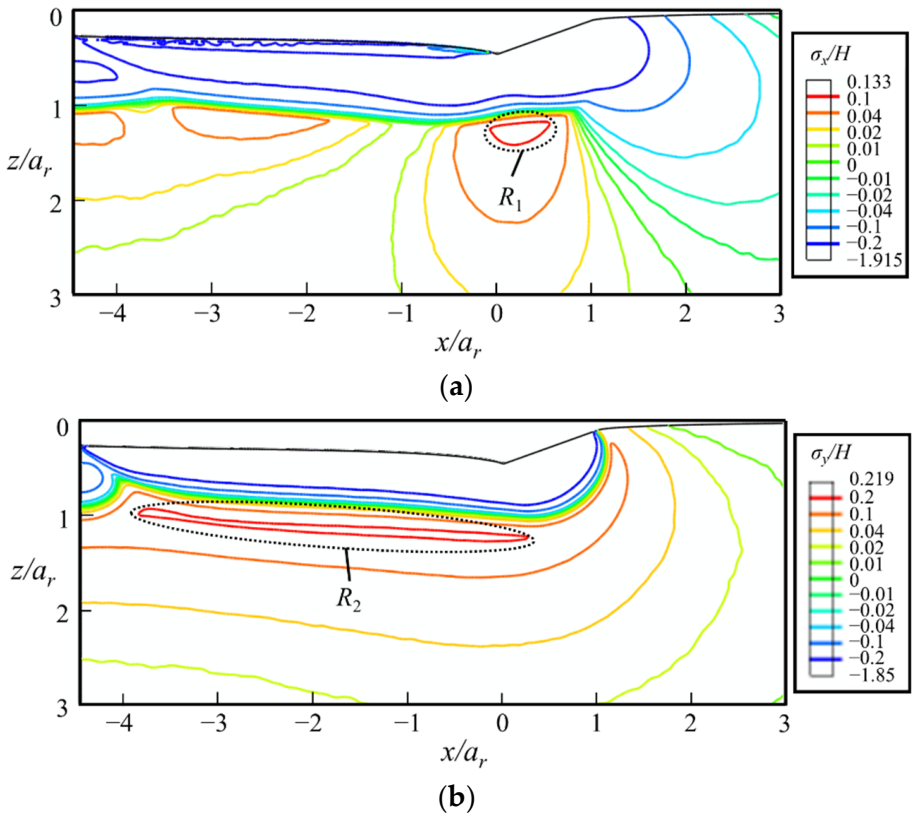

Figure 16. *Cont.*

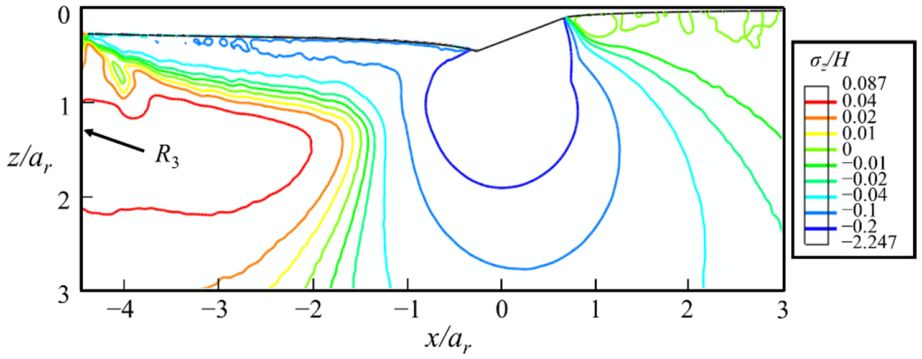

(**c**)

Figure 16. The contours of (**a**) σ_x/H, (**b**) σ_y/H, and (**c**) σ_z/H at the end of the sliding stage ② in the xz-cross-section, where a_r = 2.24 h_{max} is the real contact radius evaluated by FEA, and H is the hardness measured by indentation tests. The indenter moves along the positive direction of the x-axis.

The maximal values of σ_x and σ_y are identified in the regions below the indenter tip just outside the elastic–plastic boundary, i.e., the regions R_1 and R_2 shown in Figure 16, respectively. They are the driving forces of median cracks. As the maximal σ_y is higher than the maximal σ_x, the median crack along the sliding direction tends to initiate prior to that along the lateral direction. The maximal value of σ_z locates at the far rear of the indenter (region R_3), which is the driving force of lateral cracks. In the sliding stage, the driving force of median cracks is higher than that of lateral cracks.

5.3.2. At the Fully-Unloaded State

After unloading, as shown in Figure 17a, the stress contours predict a high σ_y on the sample surface at the front of the indenter (region R_4), which is the driving force of radial cracks along the sliding direction, i.e., the radial crack 1 in Figure 18a. σ_y at the bottom of the yield region remains nearly unchanged after unloading. Therefore, median cracks along the sliding direction remain open in the unloading stage if they initiate in the sliding stage. The maximal σ_z increases from 0.087H to 0.137H during the unloading process. This indicates that the lateral crack emerges more easily in the unloading stage compared with the sliding stage.

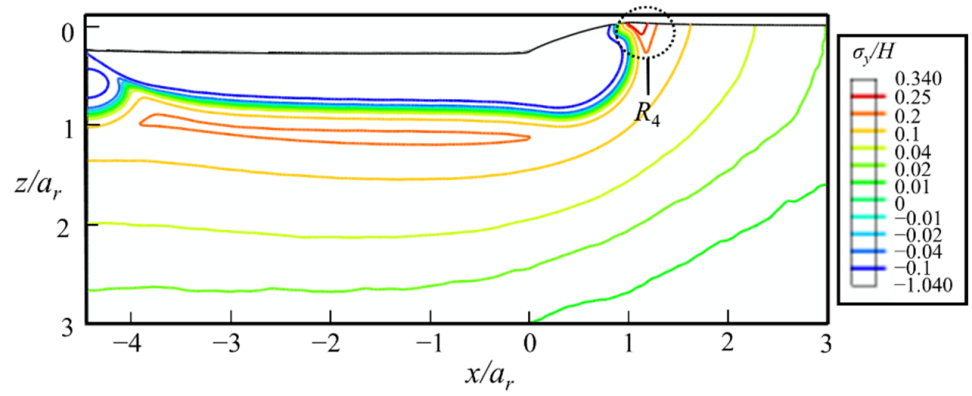

(**a**)

Figure 17. *Cont.*

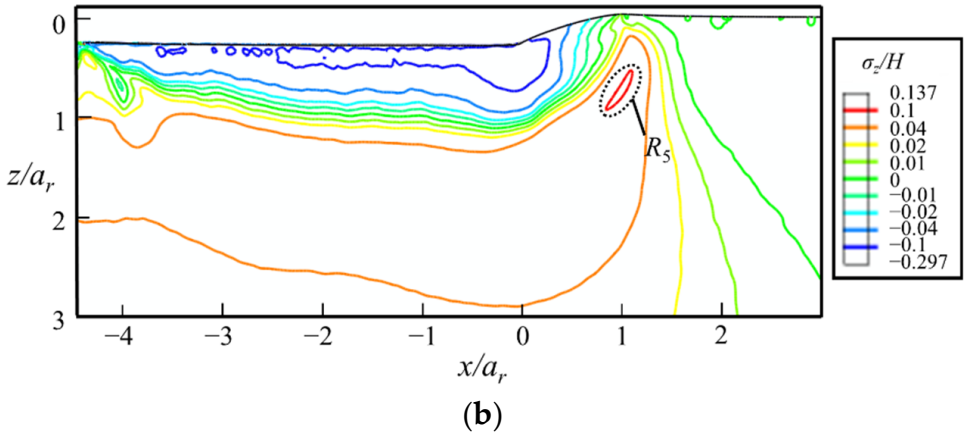

Figure 17. The contours of (**a**) σ_y/H and (**b**) σ_z/H at the fully unloaded state in the xz-cross-section predicted by FEA. The indenter moves along the positive direction of x-axis.

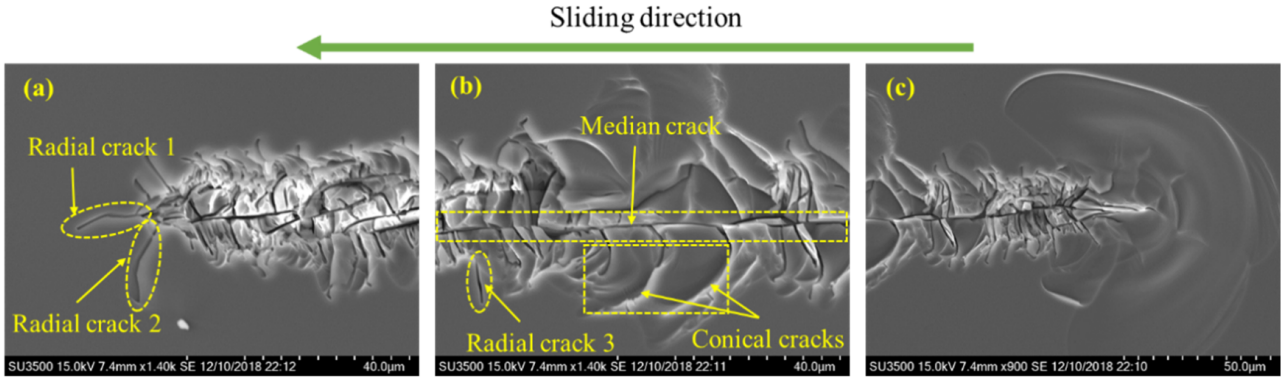

Figure 18. The SEM images of the impression at the (**a**) end, (**b**) middle, and (**c**) start of the edge-forward Berkovich scratching, under the normal load of 600 mN.

5.3.3. Maximum Principal Stress

The contours of σ_1/H shown in Figure 19 indicate that the median crack along the sliding direction tends to be the first crack to appear during the sliding stage. It initiates below the yield region at the rear of the indenter, i.e., in the region R_2. Once initiated in the xz-cross-section, the median crack propagates along the sliding direction during scratching. As the value of σ_1 in region R_3 is smaller than that in region R_2, the initiation load of median crack under indentation is higher than that under scratching. This is consistent with experimental observations. Though median crack is absent during indentation tests under the normal load of 40 N [39], it is observed during scratching tests under the normal load of 600 mN, as shown in Figure 18b. During the unloading stage, radial cracks may initiate from the sample surface at the front of the indenter, i.e., region R_4, as shown in Figure 18a. As σ_y in region R_4 is small before unloading, and significantly increases during the unloading process, radial cracks tend to emerge in the unloading stage. If both radial and median cracks form, they coalesce to form a big median–radial crack that penetrates through the entire yield region, as verified by the experiments (see Figure 18).

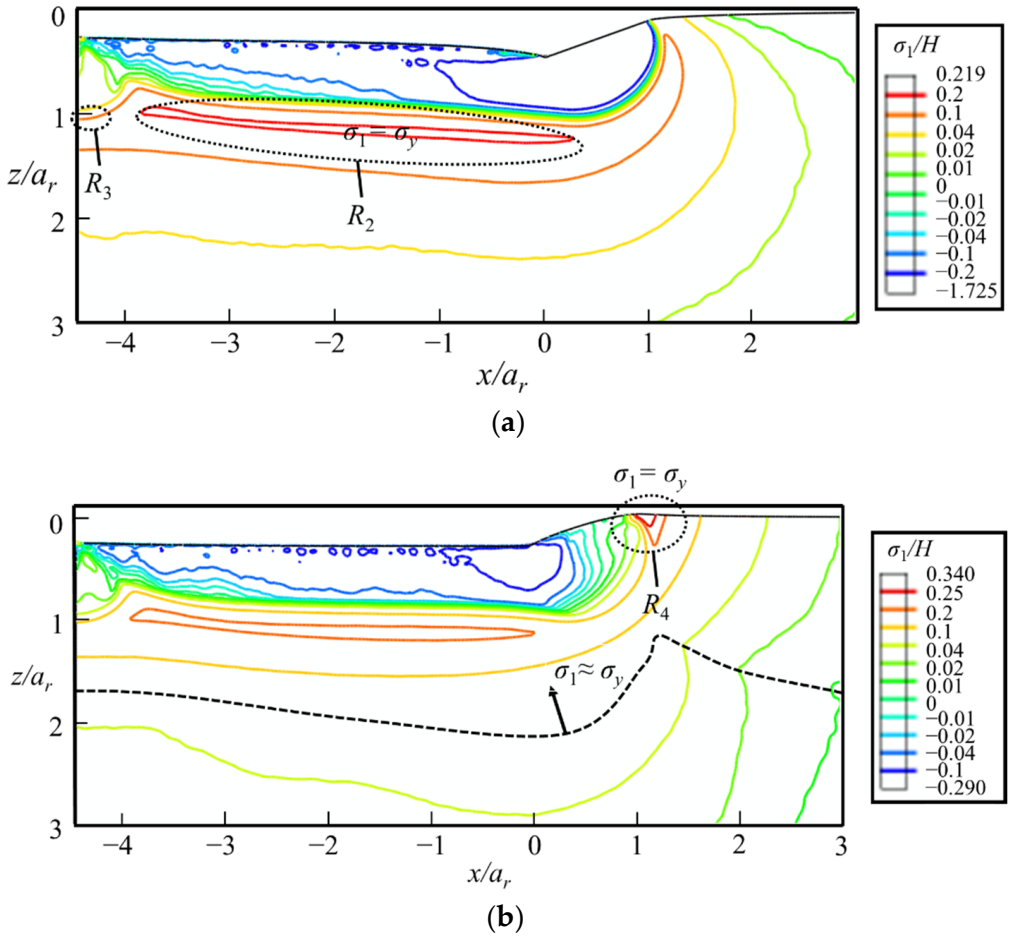

Figure 19. The contours of σ_1/H at the (**a**) fully loaded and (**b**) fully unloaded states in the *xz*-cross-section. The thick dash line is the boundary between $\sigma_1 \approx \sigma_y$ and $\sigma_1 \approx \sigma^*$, where σ^* is the in-plane principal stress.

6. Conclusions

This study developed three-dimensional finite element models of scratching on fused silica with 70.3° conical and Berkovich indenters. A refined elliptical model was used to consider the influence of densification on elastic properties and the saturation of densification with hydrostatic pressure. By analyzing the predicted scratching hardness, plastic deformation, and stress fields, the following conclusions are obtained:

(1) The tangential hardness is slightly larger than the scratching hardness, and their ratio linearly increases with the adhesion friction coefficient *f*. The scratching hardness for an edge-leading Berkovich indenter is nearly independent of *f*, because the friction increases both the contact area and the normal force. By contrast, the scratching hardness for a conical indenter linearly decreases with *f*. These findings are helpful to model the friction-affected forces induced by scratching;

(2) The densification effect should not be ignored if one aims for a damage-free process in fabrication. It is found that the material's densification under scratching is bigger than that under indentation. This indicates that the prediction accuracy of the sliding stress analyses can be improved if the material's densification is properly integrated into the modelling, e.g., replacing the spherical/cylindrical plastic zone with an ellipsoid/cylindroid, and considering the embedding of the plastic zone center;

(3) Median cracks along the sliding direction tend to be the first cracks that emerge in the sliding stage. Radial cracks may initiate under a smaller load in the sample surface at the front of the indenter during the unloading stage. Radial and median cracks coalesce to form a big median–radial crack that penetrates through the entire yield region.

Author Contributions: Conceptualization, C.L. and L.Z.; methodology, C.L., L.S., and X.W.; validation, C.L. and D.D.; formal analysis, C.L. and Y.M.; writing—original draft preparation, C.L.; writing—review and editing, L.Z. and C.W.; supervision, J.D.; project administration, J.D. and Z.C. All authors have read and agreed to the published version of the manuscript.

Funding: This research was funded by the Fellowship of China National Postdoctoral Program for Innovative Talents, grant number BX20200268; the National Natural Science Foundation of China, grant number 51720105016; the Research Project of State Key Laboratory of Mechanical System and Vibration in China, grant number MSV202103; Key Research and Development Projects of Shaanxi Province in China, grant number 2021GXLH-Z-051; the Guangdong Specific Discipline Project, grant number 2020ZDZX2006; and the Shenzhen Key Laboratory of Cross-scale Manufacturing Mechanics Project, grant number ZDSYS20200810171201007.

Data Availability Statement: Some or all data, models, or codes generated or used during the study are available from the corresponding author by request.

Conflicts of Interest: The authors declare no conflict of interest.

References

1. Campbell, J.H.; Hawley-Fedder, R.A.; Stolz, C.J.; Menapace, J.A.; Borden, M.R.; Whitman, P.K.; Yu, J.; Runkel, M.; Riley, M.O.; Feit, M.D.; et al. NIF optical materials and fabrication technologies: An overview. In Proceedings of the Optical Engineering at the Lawrence Livermore National Laboratory II: The National Ignition Facility, San Jose, CA, USA, 25–29 January 2004; pp. 84–101.
2. Gray, P.; Ciattaglia, E.; Dupuy, C.; Gago, F.; Guisard, S.; Marrero, J.; Ridings, R.; Wright, A. E-ELT Assembly, Integration, and Technical Commissioning Plans. In Proceedings of the Ground-Based and Airborne Telescopes VI, Edinburgh, UK, 26 June–1 July 2016.
3. Hrdina, K.E.; Duran, C.A. ULE®Glass with Improved Thermal Properties for EUVL Masks and Projection Optics Substrates. *Int. J. Appl. Glas. Sci.* **2014**, *5*, 82–88. [CrossRef]
4. Hergenhan, G.; Taubert, J.; Grimm, D.; Tilke, M.; Panitz, M.; Ziener, C. *Realization of Thermally Stable Transmissive Optical Elements for the EUV Wavelength Range*; SPIE: Bellingham, WA, USA, 2020; Volume 11323.
5. Zhao, L.-J.; Cheng, J.; Chen, M.-J.; Yuan, X.-D.; Liao, W.; Yang, H.; Liu, Q.; Wang, H.-J. Development of Integrated Multi-Station System to Precisely Detect and Mitigate Surface Damage on Fused Silica Optics. *Int. J. Precis. Eng. Manuf.* **2021**, *22*, 95–105. [CrossRef]
6. Malkin, S.; Hwang, T. Grinding mechanisms for ceramics. *CIRP Ann.* **1996**, *45*, 569–580. [CrossRef]
7. Suratwala, T.I.; Steele, W.A.; Wong, L.L.; Tham, G.C.; Destino, J.F.; Miller, P.E.; Ray, N.J.; Menapace, J.A.; Feigenbaum, E.; Shen, N. Subsurface mechanical damage correlations after grinding of various optical materials. *Opt. Eng.* **2019**, *58*, 092604. [CrossRef]
8. Hertz, H. Über die Berührung fester elastischer Körper. *J. Reine Angew. Math.* **1882**, *92*, 22.
9. Hill, R.; Lee, E.H.; Tupper, S.J. The theory of wedge indentation of ductile materials. *Proc. R. Soc. Lond. Ser. A Math. Phys. Sci.* **1947**, *188*, 273–289.
10. Johnson, K.L. The correlation of indentation experiments. *J. Mech. Phys. Solids* **1970**, *18*, 115–126. [CrossRef]
11. Lawn, B.R.; Evans, A.G.; Marshall, D.B. Elastic/plastic indentation damage in ceramics: The median/radial crack system. *J. Am. Ceram. Soc.* **1980**, *63*, 574–581. [CrossRef]
12. Bruns, S.; Uesbeck, T.; Fuhrmann, S.; Tarragó Aymerich, M.; Wondraczek, L.; de Ligny, D.; Durst, K. Indentation densification of fused silica assessed by raman spectroscopy and constitutive finite element analysis. *J. Am. Ceram. Soc.* **2020**, *103*, 3076–3088. [CrossRef]
13. Yoffe, E.H. Elastic Stress-Fields Caused by Indenting Brittle Materials. *Philos. Mag. A* **1982**, *46*, 617–628. [CrossRef]
14. Li, C.; Zhang, L.; Sun, L.; Yang, S.; Wu, C.; Long, X.; Ding, J.; Jiang, Z. A quantitative analysis of the indentation fracture of fused silica. *J. Am. Ceram. Soc.* **2019**, *102*, 7264–7277. [CrossRef]
15. Hamilton, G.M.; Goodman, L.E. The stress field created by a circular sliding contact. *J. Appl. Mech.* **1966**, *33*, 371–376. [CrossRef]
16. Ahn, Y.; Farris, T.N.; Chandrasekar, S. Sliding microindentation fracture of brittle materials: Role of elastic stress fields. *Mech. Mater.* **1998**, *29*, 143–152. [CrossRef]
17. Wang, W.; Yao, P.; Wang, J.; Huang, C.; Kuriyagawa, T.; Zhu, H.; Zou, B.; Liu, H. Elastic stress field model and micro-crack evolution for isotropic brittle materials during single grit scratching. *Ceram. Int.* **2017**, *43*, 10726–10736. [CrossRef]
18. Yao, L.; Zhang, L.; Ge, P.; Gao, Y.; Wang, H. Study on nucleation and propagation of median cracks generated by scratching single crystal silicon. *Mater. Sci. Semicond. Process.* **2020**, *105*, 104691. [CrossRef]
19. Lee, K.; Marimuthu, K.P.; Kim, C.-L.; Lee, H.J.T.I. Scratch-tip-size effect and change of friction coefficient in nano/micro scratch tests using XFEM. *Tribol. Int.* **2018**, *120*, 398–410. [CrossRef]
20. Arjmandi, M.; Ramezani, M. Finite element modelling of sliding wear in three-dimensional textile hydrogel composites. *Tribol. Int.* **2019**, *133*, 88–100. [CrossRef]
21. Asqari, M.A.; Akbari, J. Investigation of cohesive FE modeling to predict crack depth during deep-scratching on optical glasses. *Ceram. Int.* **2018**, *44*, 16781–16790. [CrossRef]

22. Shim, S.; Oliver, W.C.; Pharr, G.M. A comparison of 3D finite element simulations for Berkovich and conical indentation of fused silica. *Int. J. Surf. Sci. Eng.* **2007**, *1*, 259–273. [CrossRef]
23. Imaoka, M.; Yasui, I. Finite element analysis of indentation on glass. *J. Non-Cryst. Solids* **1976**, *22*, 315–329. [CrossRef]
24. Gadelrab, K.R.; Bonilla, F.A.; Chiesa, M. Densification modeling of fused silica under nanoindentation. *J. Non-Cryst. Solids* **2012**, *358*, 392–398. [CrossRef]
25. Xin, K.; Lambropoulos, J.C. Densification of fused silica: Effects on nanoindentation. In Proceedings of the International Symposium on Optical Science and Technology, San Diego, CA, USA, 30 July–4 August 2000; Volume 4102, pp. 112–121. [CrossRef]
26. Kermouche, G.; Barthel, E.; Vandembroucq, D.; Dubujet, P. Mechanical modelling of indentation-induced densification in amorphous silica. *Acta Mater.* **2008**, *56*, 3222–3228. [CrossRef]
27. Bruns, S.; Johanns, K.E.; Rehman, H.U.; Pharr, G.M.; Durst, K. Constitutive modeling of indentation cracking in fused silica. *J. Am. Ceram. Soc.* **2017**, *100*, 1928–1940. [CrossRef]
28. Li, C.; Zhang, L.; Sun, L.; Wu, C.; Duan, D.; Lin, Q.; Ding, J.; Jiang, Z. A finite element study on the effects of densification on fused silica under indentation. *Ceram. Int.* **2020**, *46*, 26861–26870. [CrossRef]
29. Li, C.; Ding, J.; Zhang, L.; Wu, C.; Sun, L.; Lin, Q.; Liu, Y.; Jiang, Z. Densification effects on the fracture in fused silica under Vickers indentation. *Ceram. Int.* **2021**, *48*, 9330–9341. [CrossRef]
30. Fang, X.; Li, C.; Sun, L.; Sun, H.; Jiang, Z. Hardness and friction coefficient of fused silica under scratching considering elastic recovery. *Ceram. Int.* **2020**, *46*, 8200–8208. [CrossRef]
31. Menapace, J.A.; Davis, P.J.; Steele, W.A.; Wong, L.L.; Suratwala, T.I.; Miller, P.E. MRF applications: Measurement of process-dependent subsurface damage in optical materials using the MRF wedge technique. In Proceedings of the Boulder Damage Symposium XXXVII: Annual Symposium on Optical Materials for High Power Lasers, Boulder, CO, USA, 19–21 September 2005.
32. Broitman, E. Indentation Hardness Measurements at Macro-, Micro-, and Nanoscale: A Critical Overview. *Tribol. Lett.* **2017**, *65*, 23. [CrossRef]
33. Brookes, C.A. Plastic Deformation and Anisotropy in the Hardness of Diamond. *Nature* **1970**, *228*, 660–661. [CrossRef]
34. Li, K.; Shapiro, Y.; Li, J.C.M. Scratch test of soda-lime glass. *Acta Mater.* **1998**, *46*, 5569–5578. [CrossRef]
35. Chamani, H.R.; Ayatollahi, M.R. The effect of Berkovich tip orientations on friction coefficient in nanoscratch testing of metals. *Tribol. Int.* **2016**, *103*, 25–36. [CrossRef]
36. Cai, X. Effect of friction in indentation hardness testing: A finite element study. *J. Mater. Sci. Lett.* **1993**, *12*, 301–302. [CrossRef]
37. Feng, G.; Qu, S.; Huang, Y.; Nix, W.D. An analytical expression for the stress field around an elastoplastic indentation/contact. *Acta Mater.* **2007**, *55*, 2929–2938. [CrossRef]
38. Rouxel, T.; Ji, H.; Hammouda, T.; Moreac, A. Poisson's ratio and the densification of glass under high pressure. *Phys. Rev. Lett.* **2008**, *100*, 225501. [CrossRef] [PubMed]
39. Cook, R.F.; Pharr, G.M. Direct Observation and Analysis of Indentation Cracking in Glasses and Ceramics. *J. Am. Ceram. Soc.* **1990**, *73*, 787–817. [CrossRef]